

Implications of σ -cut potential on Antikaon condensates in neutron stars

Prashant Thakur¹, Yashmitha Kumaran², Lakshana Sudarsan^{3,5}, Krishna Kunnampullu^{4,5}, B. K. Sharma⁵, and T. K. Jha¹

¹*Department of Physics, BITS-Pilani, K. K. Birla Goa Campus, Goa 403726, India*

²*Instituto de Astronomía, Universidad Nacional Autónoma de México, AP 70-264, Ciudad de México 04510, México*

³*Department of Mathematics, Aston School of Engineering, Aston University, Birmingham, B4 7ET, UK*

⁴*School of Geography, Geology and the Environment College of Science and Engineering, University of Leicester, Leicester, LE1 7RH, UK*

⁵*Department of Physics, Amrita School of Physical Sciences, Amrita Vishwa Vidyapeetham, Coimbatore 641112, India*

We investigate the properties of neutron stars with antikaon condensation in the framework of the Relativistic Mean-Field (RMF) model with a σ -cut potential. The well-known RMF models, TM1 and TM1e, are used to analyze the structure and composition of neutron stars. The antikaon condensation part of the equation of state (EoS) is constrained from the experimental data of K^- atomic and kaon-nucleon scattering. The σ -cut potential, which is known to make the EoS stiffer at high densities, is modulated by a free parameter f_s . Our present analysis suggests that one can obtain neutron star configurations heavier than $2M_\odot$ with antikaon condensates in most cases for $f_s = 0.6$. The antikaon phase transition is a second-order for $f_s = 0.6$ for both TM1 and TM1e parameter sets. The calculated global properties of neutron stars with antikaon condensates i.e., mass and radius seem to be in reasonable agreement with other theoretical and observational data.

I. INTRODUCTION

Neutron stars serve as a pristine astrophysical laboratory, offering a unique opportunity to investigate nuclear matter under extreme densities inaccessible in terrestrial labs [1–3]. Their composition and properties are governed by the equation of state (EoS), which describes the behavior of matter under a wide range of densities, from a few to several times the nuclear saturation density (n_0). Typically, neutron stars consist mainly of neutrons with a small proportion of protons and electrons in β -equilibrium, ensuring charge neutrality. As neutron density rises, so does the electron density and momentum. At a critical density where the electron Fermi momentum matches the rest mass of the muon, the latter one starts appearing and may be present in an appreciable amount. Further increase in density can lead to the emergence of novel phases, such as hyperons [4–9], kaon condensates [10, 11], and even quark matter [12, 13], in the dense core of neutron stars.

We embark on investigating the presence of antikaon condensates in dense nuclear matter and their effect on the underlying EoS and neutron star properties. Charge-neutral matter, primarily composed of neutrons, protons, and electrons, may also have the possibility of undergoing a transition to condensates with an increase in baryon density. The attractive K^- -nucleon interaction becomes stronger as the density increases, leading to a decrease in the effective mass m_{K^*} of antikaons. This results in a decrease in the in-medium energy of K^- -mesons, ω_{K^-} , causing s -wave K^- condensation to occur ω_{K^-} is equal to the K^- chemical potential μ_{K^-} which is also equal to the electron chemical potential μ_e in a cold catalyzed (neutrino-free) neutron star matter [14]. Above this threshold, kaons can form a sizable population, potentially suppressing the electron population. Notably, the critical density for antikaon appearance is sensitive to the optical potential in symmetric nuclear matter. Antikaon condensation has been observed in dense baryonic matter from heavy-ion collisions [15, 16], with subsequent studies exploring its occurrence in neutron stars using chiral [17–20] and relativistic mean field (RMF) models [21, 22].

Glendenning and Schaffner provided a comprehensive analysis of first-order kaon condensation within the RMF model, excluding hyperons [14]. Other investigations, employing density-dependent RMF [23, 24] and quark-meson coupling models [25–27], also explored kaon condensation's effects. These studies collectively suggest that kaon condensation is known to soften the EoS at high densities, reducing neutron star maximum mass. In contrast, recent mass measurements of pulsars, such as PSR J1614-2230 [28, 29], PSR J0348+0432 [30], and PSR J0740+6620 [31, 32], indicate masses exceeding twice that of the Sun ($M \geq 2M_\odot$). Observational data from sources like NICER and the GW170817 event [33] constrain the EoS and neutron star properties, driving the need for models that incorporate these constraints effectively.

The nuclear symmetry energy E_{sym} and its density dependence [34, 35] are crucial quantities that provide important information about neutron-rich matter at high density. They significantly impact the pressure of neutron star matter and influence properties such as the radius of neutron stars [36, 37]. Despite their significance in the equation of state (EoS), the understanding of nuclear symmetry energy and its behavior at high-density remains limited. Various studies have attempted to constrain the value of E_{sym} and its high-density behavior using data from both terrestrial experiments and astrophysical observations [38–42]. A recent study reported an improved neutron skin thickness of ^{208}Pb around (0.283 ± 0.071) fm from the Lead Radius EXperiment-II (PREX-2) [43]. This measurement yielded values of E_{sym} and its slope L at nuclear saturation density n_0 of (38.1 ± 4.7) MeV and (106 ± 37) , respectively [44], which are higher than previously reported values [3]. These updated values were derived from comparisons of experimental data from finite nuclei and heavy-ion collisions with various microscopic model calculations. The models that we use and compare in the present work, TM1e [45] is an extension of the original TM1 [46], where the ω - ρ cross-coupling was introduced in the former to bring down the symmetry energy slope parameter from $L = 110.8$ MeV to $L = 40$ MeV, with an additional parameter $\Lambda_v = 0.0429$, which

agrees with the earlier reported values [3]. However, TM1 has the slope parameter $L = 110.8$ MeV which is more consistent with the recent data [43]. Therefore, these two values of L cover a wide enough range to survey the effect of symmetry energy.

In our previous work with RMF models [47], we studied pure nucleonic and hyperon-rich neutron star matter. Our findings indicate that the effect of Λ_v coupling has a more significant impact on tidal deformability compared to the mass and radius of a neutron star when the value of f_s is fixed. Therefore, in this work, we aim to investigate how the σ -cut potential affects neutron star properties through f_s and the symmetry energy through Λ_v in the presence of antikaon condensation. The TM1 [46] and TM1e [45] parameter sets were chosen for the present analysis, with the TM1e set being particularly relevant due to the Λ_v coupling which is crucial for tidal deformability. In ref. [48], it is demonstrated that f_s must be higher than 0.55 in the TM1 model to maintain the properties of finite nuclei without being affected by the σ -cut potential. Therefore, we have set $f_s = 0.6$ for the present analysis.

The criteria of large maximum neutron star masses, small stellar radii, and a low tidal deformability as determined from the GW170817 binary NS merger pose a significant challenge for nuclear models of the Equation of State (EoS), particularly those incorporating non-nucleonic matter inside the neutron star. As already mentioned, the f_s and Λ_v coupling control the mass, radius, and tidal deformability, respectively. The Λ_v coupling is fixed by experimental and observational constraints [49]. The $f_s = 0.6$ for TM1 is fixed without changing the ground-state properties of finite nuclei with the original TM1 interaction and the constraints of observed massive neu-

tron stars [48]. In ref. [48], they studied neutron stars with or without hyperon core, so this work focuses on antikaon condensation in pure nucleonic neutron star matter. It is worth investigating whether the $f_s = 0.6$ has a similar impact on antikaon condensation as hyperonic neutron star matter.

The paper is structured as follows: Section II outlines the RMF model with a σ -cut potential and the stellar equations for neutron stars. In Section III, we analyze the influence of the σ -cut potential on nuclear matter and neutron star properties with antikaon condensation. Finally, Section IV offers a summary and conclusions of our findings.

II. FORMALISM

In this section, we provide a brief description of the main features of the baryonic model used to evaluate the equation of state of neutron stars and the procedure for obtaining stellar properties. Specifically, we investigate the aspects of tidal deformability with condensates and compare them with the GW analysis.

A. Equation of State

We use the RMF models, namely the TM1 and TM1e to describe the equation of state (EoS) for nucleonic matter with antikaon condensation. The TM1e model is an extension of the TM1 parameterization with the Λ_v coupling. The Λ_v coupling term is essential to modify the density dependence of the symmetry energy [50]. We also include $U_{cut}(\sigma)$ to make EoS stiffer at high density. The Lagrangian density [49] with $U_{cut}(\sigma)$ for nucleonic degrees of freedom is given by:

$$\begin{aligned} \mathcal{L}_N = & \sum_{i=p,n} \bar{\Psi}_i \left[i\gamma_\mu \partial^\mu - (M_N + g_{\sigma N} \sigma) - \gamma_\mu \left(g_{\omega N} \omega^\mu + \frac{g_{\rho N}}{2} \tau_a \rho^{a\mu} \right) \right] \Psi_i + \frac{1}{2} \partial_\mu \sigma \partial^\mu \sigma - \frac{1}{2} m_\sigma^2 \sigma^2 - \frac{1}{3} g_2 \sigma^3 - \frac{1}{4} g_3 \sigma^4 \\ & - \frac{1}{4} W_{\mu\nu} W^{\mu\nu} + \frac{1}{2} m_\omega^2 \omega_\mu \omega^\mu + \frac{1}{4} c_3 (\omega_\mu \omega^\mu)^2 - \frac{1}{4} R_{\mu\nu}^a R^{a\mu\nu} + \frac{1}{2} m_\rho^2 \rho_\mu^a \rho^{a\mu} \\ & + \Lambda_v (g_{\omega N}^2 \omega_\mu \omega^\mu) (g_{\rho N}^2 \rho_\mu^a \rho^{a\mu}) - U_{cut}(\sigma) \end{aligned} \quad (1)$$

The antisymmetric field tensors $W^{\mu\nu}$ and $R^{a\mu\nu}$ correspond to the fields ω^μ and $\rho^{a\mu}$, respectively. We incorporate the ω - ρ coupling term as outlined in [51], which is crucial for altering the symmetry energy slope. In the RMF model, the meson fields are considered as classical fields, and the field operators are substituted with their expectation values, i.e., $\sigma = \langle \sigma \rangle$, $\omega = \langle \omega^0 \rangle$ and $\rho = \langle \rho^{30} \rangle$, respectively. The $U_{cut}(\sigma)$ has a logarithmic form as [52], which only affects the σ -field at high density [48] and is given by:

$$U_{cut}(\sigma) = \alpha \ln[1 + \exp\{\beta(-g_{\sigma N} \sigma / M_N - f_s)\}] \quad (2)$$

where $\alpha = m_\pi^4$ and $\beta = 120$ [52] to make the equation of state (EoS) stiffer at high density. The factor f_s is a free param-

eter and we take $f_s = 0.6$ for our calculation. As the density increases, kaon condensation occurs in the interior of neutron stars. The Lagrangian for same is as follows:

$$\mathcal{L}_K = D_\mu^* K^* D^\mu K - m_K^{*2} K^* K \quad (3)$$

The covariant derivative is given by $D^\mu = \partial^\mu + i g_{\omega K} \omega_\mu + \frac{i g_{\rho K}}{2} \tau_K \cdot \rho_\mu$ and the effective mass of the kaon is $m_K^* = m_K + g_{\sigma K} \sigma$. The vector couplings $g_{\omega K}$ and $g_{\rho K}$, which represents the interactions between vector meson and the kaon, are determined by the SU(3) symmetry as $g_{\omega K} = g_{\omega N} / 3$ and $g_{\rho K} = g_{\rho N}$. The scalar coupling $g_{\sigma K}$ is determined by the optical potential of the K^- in saturated nuclear matter:

$$U_{K^-}(n_0) = g_{\sigma K} \sigma(n_0) - g_{\omega K} \omega(n_0) \quad (4)$$

TABLE I: The coupling constants of the TM1 and TM1e Models.

Model	$g_{\sigma N}$	$g_{\omega N}$	$g_{\rho N}$	$g_2(fm^{-1})$	g_3	c_3	Λ_v
TM1	10.0289	12.6139	9.2644	-7.2325	0.6183	71.3075	0.0000
TM1e	10.0289	12.6139	13.9714	-7.2325	0.6183	71.3075	0.0429

TABLE II: The coupling constants for the antikaons to σ -meson i.e., $g_{\sigma K}$, for different values of U_{K^-} at saturation density n_0 for TM1.

$U_{K^-}(MeV)$	-100	-120	-140	-160
TM1	0.2537	0.8384	1.4241	2.0098

where n_0 is the symmetric nuclear matter saturation density and eq.(8) defines the kaon-nucleon interaction. It is to be noted that the difference between TM1 and TM1e lies in the value of $g_{\rho N}$ and Λ_v couplings as shown in Table I [45]. As these couplings do not have any role to play in symmetric nuclear matter the kaon-nucleon interaction remains the same for both TM1 and TM1e. The coupling constants for antikaon to the σ -meson, i.e., $g_{\sigma K}$ for various values of antikaon optical potential depths U_{K^-} at saturation density n_0 , which is $0.145 fm^{-3}$ for TM1 are given in Table II.

Several experimental studies have demonstrated that kaons experience a repulsive interaction at saturation density in nuclear matter, while antikaons experience an attractive potential [53, 54]. The depth of the attractive potential for antikaons is predicted to be $U_{K^-}(n_0) = -120$ MeV at n_0 by Waas and Weise [55], and $U_{K^-}(n_0) = -100$ MeV was calculated by coupled channel calculations at finite density [56]. Self-consistent calculations using a chiral Lagrangian [57, 58] and coupled channel calculations, including a modified self-energy of the kaon [59], predict that the depth of the attractive potential for antikaons is approximately -80 MeV to -50 MeV at nuclear saturation density. According to a hybrid model [60], the value of the K^- optical potential is estimated to be around 180 ± 20 MeV. In this study, we performed calculations using optical potentials ranging from -160 MeV to -100 MeV.

From Eq.(3), we can derive the Euler-Lagrangian equation for the kaon, as well as the dispersion relation for the Bose-Einstein condensation of the K^- which is given by:

$$\omega_{K^-} = m_K^* - g_{\omega K} \omega - \frac{g_{\rho K}}{2} \rho \quad (5)$$

Using Eq.(5), the kaon energy ω_{K^-} can be calculated as a function of density. As the density increases, the electron chemical potential, μ_e also increases, and ω_{K^-} decreases. When ω_{K^-} decreases to a certain value such that $\mu_{K^-} = \mu_e$, the K^- starts appearing in the matter, a phase which is usually referred to as antikaon condensation.

The presence of K^- modifies the field equations for σ , ω , and ρ -mesons, which can be expressed as:

$$m_\sigma^2 \sigma + g_2 \sigma^2 + g_3 \sigma^3 + U'_{cut}(\sigma) = -g_{\sigma N} (n_p^s + n_n^s) - g_{\sigma K} n_K \quad (6)$$

$$m_\omega^2 \omega + c_3 \omega^3 + 2\Lambda_v g_{\omega N}^2 g_{\rho N}^2 \rho^2 \omega = g_{\omega N} (n_p + n_n) - g_{\omega K} n_K \quad (7)$$

$$m_\rho^2 \rho + 2\Lambda_v g_{\omega N}^2 g_{\rho N}^2 \omega^2 \rho = \frac{g_{\rho N}}{2} (n_p - n_n) - \frac{g_{\sigma K}}{2} n_K \quad (8)$$

Here, n_i^s , n_i , and $n_K = 2(\omega_{K^-} + g_{\omega K} \omega + \frac{g_{\sigma K}}{2} \rho) K^* K$ are the scalar density, number density of species i , and kaon density, respectively. The derivative of $U_{cut}(\sigma)$ [48] is given by:

$$U'_{cut}(\sigma) = \frac{\alpha \beta g_{\sigma N}}{M_N} \frac{1}{[1 + \exp\{-\beta(-g_{\sigma N} \sigma / M_N - f_s)\}]} \quad (9)$$

The total energy density \mathcal{E} of the charge neutral β -equilibrated neutron star matter with kaon condensation can be represented as

$$\begin{aligned} \mathcal{E} = & \sum_{i=p,n} \frac{1}{\pi^2} \int_0^{k_{F_i}} dk k^2 \sqrt{k^2 + M_N^{*2}} + \frac{1}{2} m_\sigma^2 \sigma^2 + \frac{1}{3} g_2 \sigma^3 \\ & + \frac{1}{4} g_3 \sigma^4 + U_{cut}(\sigma) + \frac{1}{2} m_\omega^2 \omega^2 + \frac{3}{4} c_3 \omega^4 + \frac{1}{2} m_\rho^2 \rho^2 \\ & + 3\Lambda_v (g_{\omega N}^2 \omega^2) (g_{\rho N}^2 \rho^2) + \mathcal{E}_{K^-} + \sum_L \mathcal{E}_L \end{aligned} \quad (10)$$

and similarly the total pressure can be calculated as

$$\begin{aligned} P = & \sum_{i=p,n} \frac{1}{3\pi^2} \int_0^{k_{F_i}} dk k^2 \frac{k^2}{\sqrt{k^2 + M_N^{*2}}} - \frac{1}{2} m_\sigma^2 \sigma^2 - \frac{1}{3} g_2 \sigma^3 \\ & - \frac{1}{4} g_3 \sigma^4 - U_{cut}(\sigma) + \frac{1}{2} m_\omega^2 \omega^2 + \frac{1}{4} c_3 \omega^4 + \frac{1}{2} m_\rho^2 \rho^2 \\ & + \Lambda_v (g_{\omega N}^2 \omega^2) (g_{\rho N}^2 \rho^2) + \sum_L P_L \end{aligned} \quad (11)$$

In Eq. (10) \mathcal{E}_{K^-} is the energy density contributed by kaon condensation and is given by:

$$\mathcal{E}_{K^-} = 2m_K^{*2} K^* K = m_K^{*2} n_K \quad (12)$$

Since the antikaon is an (s-wave) Bose condensate, it does not directly contribute to the pressure. However, the presence of the antikaon affects the fields, which in turn affects the pressure. The energy density and pressure from leptons (i.e., electrons and muons) are denoted by \mathcal{E}_L and P_L , respectively.

B. Stellar Equations and Tidal Deformability

The mass-radius relation for a neutron star is obtained by the Tolman, Oppenheimer, and Volkoff (TOV) equation [61, 62], which is given by:

$$\frac{dP}{dr} = -\frac{G}{r} \frac{[\varepsilon + P] [M + 4\pi r^3 P]}{(r - 2GM)}, \quad (13)$$

$$\frac{dM}{dr} = 4\pi r^2 \varepsilon, \quad (14)$$

We use natural units, where $c = 1$, G , $P(r)$, and $M(r)$ represent the universal gravitational constant, pressure of a neutron star, and the enclosed gravitational mass inside a sphere of radius (r) respectively. Equations (13) and (14) are solved to determine the structural properties of a static neutron star composed of charge-neutral matter [1, 63].

The tidal deformability parameter λ is defined as [64–67]:

$$Q_{ij} = -\lambda \mathcal{E}_{ij}, \quad (15)$$

where Q_{ij} represents the induced quadrupole moment of a star in a binary system as a result of the static external tidal field \mathcal{E}_{ij} from the companion star. The parameter λ can be defined in relation to the dimensionless quadrupole tidal Love number k_2 as:

$$\lambda = \frac{2}{3} k_2 R^5, \quad (16)$$

where R represents the radius of the NS. The value of k_2 typically falls in the range of approximately 0.05 to 0.15 [65, 66, 68] for NSs and is dependent on the stellar structure. This quantity can be determined using the following expression [65],

$$k_2 = \frac{8C^5}{5} (1 - 2C)^2 [2 + 2C(y_R - 1) - y_R] \times \left\{ 2C [6 - 3y_R + 3C(5y_R - 8)] + 4C^3 [13 - 11y_R + C(3y_R - 2) + 2C^2(1 + y_R)] + 3(1 - 2C)^2 [2 - y_R + 2C(y_R - 1)] \log(1 - 2C) \right\}^{-1} \quad (17)$$

where $C (\equiv M/R)$ is the compactness parameter of the star with mass M . The value of $y_R (\equiv y(R))$ can be found by solving the following differential equation

$$r \frac{dy(r)}{dr} + y(r)^2 + y(r)F(r) + r^2 Q(r) = 0, \quad (18)$$

with

$$F(r) = \frac{r - 4\pi r^3 (\varepsilon(r) - P(r))}{r - 2M(r)}, \quad (19)$$

$$Q(r) = \frac{4\pi r \left(5\varepsilon(r) + 9P(r) + \frac{\varepsilon(r) + P(r)}{\partial P(r)/\partial \varepsilon(r)} - \frac{6}{4\pi r^2} \right)}{r - 2M(r)} - 4 \left[\frac{M(r) + 4\pi r^3 P(r)}{r^2 (1 - 2M(r)/r)} \right]^2. \quad (20)$$

In the previous equations, $M(r)$ represents the mass enclosed within the radius r , while $\varepsilon(r)$ and $P(r)$ represent the energy density and pressure, respectively, in terms of the radial coordinate r of a star. These quantities are calculated within the chosen nuclear matter model to describe the stellar EoS. For a given EoS, Eq.(18) can be integrated together with the Tolman-Oppenheimer-Volkoff equations using the initial boundary conditions $y(0) = 2$, $P(0) = P_c$ and $M(0) = 0$, where $y(0)$, P_c and $M(0)$ are the dimensionless quantity, pressure and mass at the center of the NS, respectively. The dimensionless tidal deformability can then be defined as $\Lambda = \frac{2}{3} k_2 C^{-5}$.

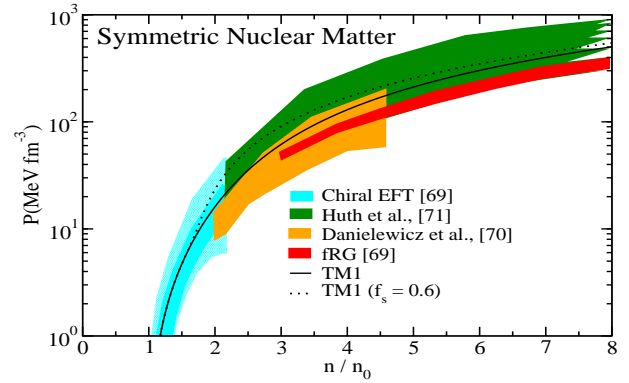


FIG. 1: The pressure of symmetric nuclear matter as a function of nucleon number density n (in units of n_0) is shown for TM1 and TM1 with $f_s = 0.6$, along with additional constraints (as mentioned in the text), represented by shaded regions.

III. RESULTS AND DISCUSSION

We now discuss the results of our investigation of neutron stars with antikaon condensation under TM1 and TM1e interactions with and without the σ -cut potential. The impact of the σ -cut potential on the underlying pressure can be seen from Fig. 1, where we show the pressure as a function of nucleon number density (n) (in units of n_0) for symmetric nuclear matter (SNM) for TM1. Alongside other constraints are also compared from various studies such as the one from the chiral EFT (cyan band) [69], ones derived from the heavy-ion collisions data [70] (orange band), functional renormalization group (fRG) methods based on QCD by [69] (red band), and recently proposed equations of state (EoSs) from [71] (green band). It's worth noting that the pressure of symmetric nuclear matter for both TM1e and TM1 remains the same since there's no contribution from the ρ -meson in the symmetric nuclear matter. From Fig. 1, it's evident that both TM1 and TM1 with $f_s = 0.6$ are in agreement with other constraints across all values of nucleon number density (n) in symmetric nuclear matter. However, both the equation of state, i.e., TM1 and TM1 with $f_s = 0.6$ predict slightly higher pressure values compared to fRG (red band) within the density range of $3 \leq n/n_0 \leq 10$. The EoS with $f_s = 0.6$ is not consistent with the prediction from the heavy-ion collision data for SNM.

In Fig. 2, the calculated pressure of neutron star matter is plotted against the nucleon number density n (in units of n_0) for TM1 and TM1 with $f_s = 0.6$, alongside TM1e and TM1e with $f_s = 0.6$. A recent advancement in precise radius measurements was achieved by the Neutron Star Interior Composition Explorer (NICER) collaboration [72, 73], which determined the radius and mass of PSR J0030+0451 simultaneously through x-ray pulse-profile modeling. Raaijmakers et al. [74] investigated the implications of this measurement on the equation of state (EoS) by utilizing two parametrizations for the neutron star EoS (in β -equilibrium): a piecewise polytropic (PP) model with varying transition densities between the polytropes [75] and a speed of sound (CS) model based on physical considerations at both nuclear and high densities

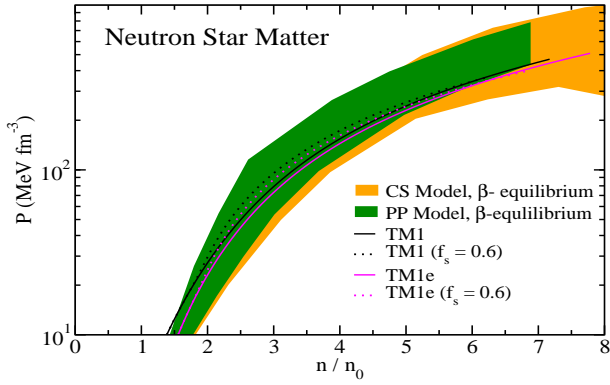


FIG. 2: The pressure of neutron star matter as a function of nucleon number density n (in units of n_0) is shown for TM1 and TM1 with $f_s = 0.6$, as well as for TM1e and TM1e with $f_s = 0.6$, along with additional constraints represented by shaded regions.

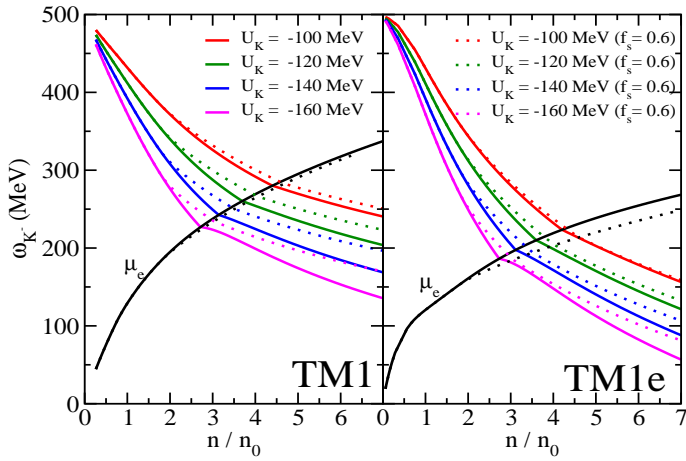


FIG. 3: The in-medium (anti)Kaon energy is plotted as a function of nucleon number density n (in units of n_0) in a neutron star with the TM1 and TM1e parameter sets without (solid line) and with (dotted line) $f_s = 0.6$ for different kaon potentials as indicated in the left and right panels, respectively. The electron chemical potential μ_e in the absence of kaons without (solid black line) and with (dotted black line) $f_s = 0.6$ is shown in both panels.

[76]. Raaijmakers et al. [77] conducted a combined analysis of these models to deduce implications on the EoS from the NICER measurement, GW170817, and the $2.14 M_\odot$. Their findings for the pressure as a function of density are depicted i.e., CS model (orange band) and PP model (green band) in Fig. 2. It is evident that TM1 and TM1e remain consistent with the CS and PP models. Introduction of the σ -cut potential $f_s = 0.6$ also maintains consistency with both CS and PP models across all values of nucleon number density (n).

The left and right panels of Figure 3 display the in-medium antikaon energy (ω_{K^-}) plotted against nucleon number density, normalized to n_0 for the models TM1 and TM1e respectively. In the left panel of figure 3, the solid lines shows the results of TM1 equation of state (EoS), while the dotted lines

illustrates the outcomes with the inclusion of a σ -cut potential with $f_s = 0.6$. From both the panels, it is evident that the energy of antikaons energy decreases with density as expected. Moreover, the curve of the electron chemical potential (μ_e) intersects the kaon energy at different densities, corresponding to different (anti)kaon potentials, marking the end of the pure hadronic phase and the onset of the condensate phase. The dotted lines in the figure illustrate the effect of the σ -cut potential on the in-medium antikaon energy, which becomes noticeable around $2n_0$ for all values of U_{K^-} . At higher densities from $2n_0$ to $7n_0$, the impact of the σ -cut potential becomes more significant for deeper values of U_{K^-} with highest effect observed for $U_{K^-} = -160$ MeV and the lowest for $U_{K^-} = -100$ MeV. The σ -cut potential is known to reduce the influence of the σ field, resulting in a stiffer antikaon energy (ω_{K^-}) at high densities, it is more pronounced for $U_{K^-} = -160$ MeV due to the higher contribution of the σ -field compared to other U_{K^-} values.

Similarly, solid lines represent the results of the TM1 equation of state (EoS), while the dotted lines illustrate the outcomes with the inclusion of a σ -cut potential with $f_s = 0.6$ in the right panel of Figure 3. In this case, the antikaon energy decreases with density for all values of U_{K^-} , and it reduces to a lower value as the density increases for a given value of U_{K^-} due to the additional Λ_v coupling as well as a larger value of g_ρ in TM1e compared to TM1. The overall effect of the σ -cut potential is more or less the same as TM1. However, the most significant effect of the σ -cut potential and symmetry energy is on the electron chemical potential (μ_e) in TM1e compared to TM1 with and without f_s . The electron chemical potential μ_e is more influenced by the isovector channel, specifically the contribution of the ρ -field compared to the σ and ω -fields. As a result, TM1e, with a higher g_ρ value and additional Λ_v coupling leads to a significant decrease in the value of μ_e after $2n_0$ for TM1e with $f_s = 0.6$ compared to TM1 with $f_s = 0.6$.

In Fig. 4, we illustrate the equation of state (EoS) by showing the variations of pressure with respect to nucleon density normalized to n_0 for different values of (anti)kaon potential U_{K^-} for TM1 (solid line) and TM1e (dashed line). The TM1e, an extension of TM1 with Λ_v coupling, results in a softer EoS at high density for all U_{K^-} values. In TM1e, antikaons appear at lower densities compared to TM1, with this difference being more pronounced for U_{K^-} values of -100 and -120 MeV. The nucleon density difference at which antikaons occur between TM1 and TM1e decreases for deeper U_{K^-} values. The phase transition of antikaons is second order for all U_{K^-} values in both TM1 and TM1e parameter sets.

Figures 5 and 6 illustrate the impact of the (anti)kaon potential on the pressure as a function of normalized baryon density for TM1 and TM1e, respectively. The solid lines in both figures represent the effect of the (anti)kaon potential on the pressure for the TM1 and TM1e parameter sets, while the dotted line in both figures shows the TM1 and TM1e with $f_s = 0.6$, respectively. It is evident from Figure 5 that the EoS becomes stiffer for TM1 with $f_s = 0.6$ compared to the TM1 parameter set. Similarly, EoS of TM1e with $f_s = 0.6$ is stiffer compared to TM1e parameter set as shown in Figure 6. The TM1e model exhibits a softer profile compared to the TM1

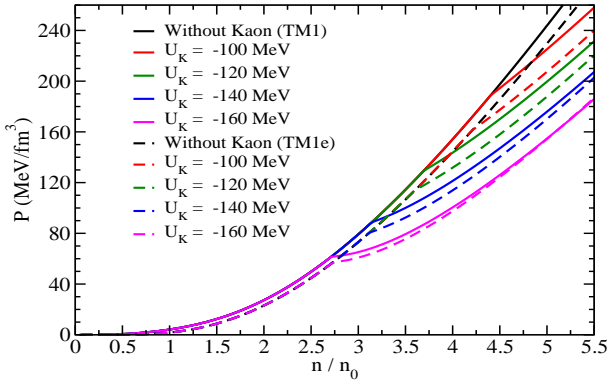


FIG. 4: Pressure (P) as a function of normalized nucleon density is plotted for TM1 (solid line) and TM1e (dashed line). The scenario without K^- (black line) is compared with pressure curves including K^- condensates for different potentials such as $U_{K^-} = -100$ MeV (red), $U_{K^-} = -120$ MeV (green), $U_{K^-} = -140$ MeV (blue), and $U_{K^-} = -160$ MeV (magenta).

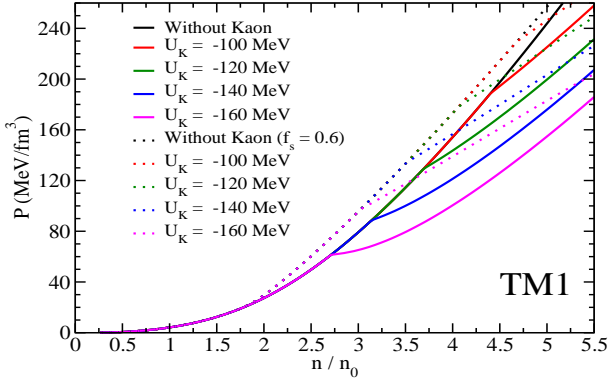


FIG. 5: Pressure (P) as a function of normalized nucleon density is plotted for TM1. The scenario without K^- (black line) is compared with pressure curves including K^- condensates for different potentials such as $U_{K^-} = -100$ MeV (red), $U_{K^-} = -120$ MeV (green), $U_{K^-} = -140$ MeV (blue), and $U_{K^-} = -160$ MeV (magenta). The dotted line shows the results by incorporating the σ -cut potential with $f_s = 0.6$.

model due to the Λ_v coupling. The effect of antikaons remains consistent with TM1, with the softest behavior observed for $U_{K^-} = -160$ MeV.

When incorporating a σ -cut potential with $f_s = 0.6$, the EoS shows slightly increased stiffness for specific U_{K^-} values compared to the counterpart as evident from both figures. The points at which the kaons begin to appear in dense matter are reflected as branching points on the pressure curve at those densities. The inclusion of the σ -cut potential delays the onset of the condensate phase, resulting in slightly stiffer pressure curves. It is important to note that from Figures 5 and 6, antikaon condensation is of second order for all the values of U_{K^-} for both TM1 and TM1e with and without σ -cut potential.

In Fig. 7, we show the particle fractions at a specific po-

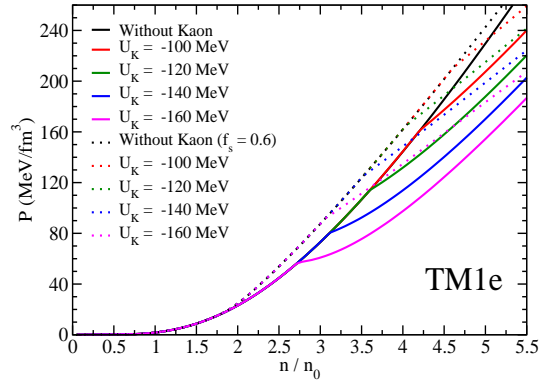


FIG. 6: Same as Fig. 5, but for TM1e.

tential value of $U_{K^-} = -120$ MeV, separately for TM1 (upper panel) and TM1e (lower panel). The associated dotted lines represents the corresponding particle fractions, when the σ -cut potential is incorporated for the two models. The analogous feature that is seen in both models is the density at which the (anti)kaons start appearing at roughly $3.7n_0$. A more or less similar delay is seen in their appearance when the σ -cut potential is incorporated. Before the emergence of K^- , the system upholds charge neutrality among protons, electrons, and muons. It becomes evident that upon the onset of K^- condensation, the system swiftly restores its charge neutrality, occurring at $\approx 3.7n_0$ for TM1 and $3.6n_0$ for TM1e, resulting in the subsequent deleptonization. Therefore, the symmetry energy has a minor impact on the emergence of K^- . However, the deleptonization happens faster in the case of TM1e in comparison. This behavior is driven by the nuclear symmetry energy, which is controlled by g_ρ and Λ_v coupling. When the antikaon condensation occurs, it increases with density, replacing leptons to maintain charge neutrality. This lowers the electron chemical potential μ_e , leading to faster deleptonization in the case of TM1e due to a larger value of g_ρ with additional Λ_v coupling. This outcome aligns with the expectation that as K^- mesons, being bosons, preferentially condense in the lowest-energy state, maintaining charge neutrality. As a result, there is an increase in the proton fraction, consequently leading to an almost isospin symmetric state at higher densities.

The mass-radius relationship for neutron stars (NS) for the two models, TM1 and TM1e, is shown in Fig. 8 and Fig. 9, with the right panel magnifying the results obtained by incorporating the σ -cut ($f_s = 0.6$) scheme with different (anti)kaon potentials. Black lines depict the baseline calculations involving neutron, proton, and lepton matter, whereas colored lines represent the effects of K^- condensates with different optical potentials. The red shaded region indicates the astrophysical constraints derived from the LIGO GW170817 event [78]. Additionally, the two-dimensional posterior distribution in the mass-radius domain obtained from NICER X-ray data for the millisecond pulsar PSR J0030+0451 is shown. Other shaded regions represent constraints from PSR J0348+0432 (cyan) [30] and PSR J0740+6620 [31, 32].

The upper and lower panels of Table III show the maximum

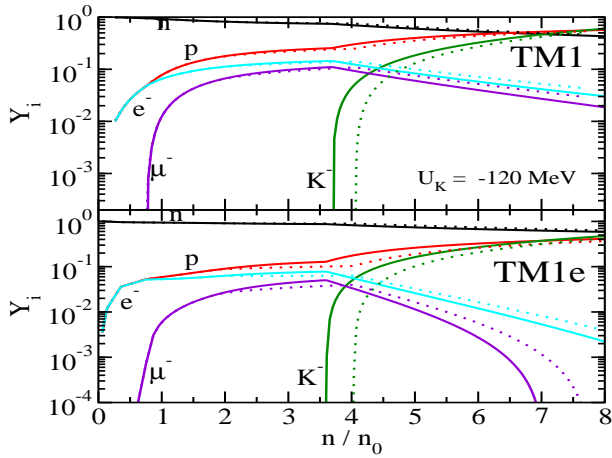


FIG. 7: Fraction of various particles in β -equilibrated neutron, proton, lepton matter including K^- condensates for $U_{K^-} = -120$ MeV as a function of normalized nucleon number density for TM1 (upper panel) and TM1e (lower panel). The associated dotted curves represent the fractions for $f_s = 0.6$.

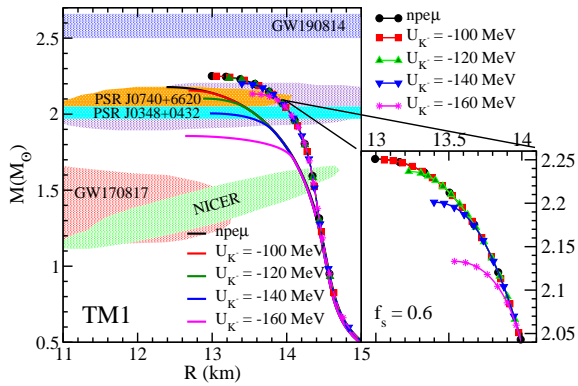


FIG. 8: The MR solution curve of the neutron star with the TM1 model. Here the solid lines represent calculations without σ -cut, while the lines with symbols are the results with σ -cut ($f_s = 0.6$) and is magnified in the adjacent figure. Black lines correspond to neutron, proton, and lepton matter, whereas other lines depict K^- condensates computed for different U_{K^-} potentials. The shaded region illustrates the available astrophysical constraints.

mass, radius, and central density for different U_{K^-} values for TM1 and TM1 with $f_s = 0.6$, respectively. Similarly, the upper and lower panels of Table IV provide the maximum mass, radius, and central density for different U_{K^-} values for TM1e and TM1e with $f_s = 0.6$, respectively. We observed that the maximum mass decreases with an increase in the depth of the (anti)kaon potential for both models (with or without σ -cut), as shown in Tables III and IV, respectively. Neutron stars composed of only nucleons and leptons (without antikaon) have the maximum masses of $2.178 M_\odot$ and $2.251 M_\odot$ for TM1 and TM1 with $f_s = 0.6$ and $2.120 M_\odot$ and $2.176 M_\odot$ for TM1e and TM1e with $f_s = 0.6$, respectively. Notably, neutron stars with antikaon remain consistent with the observed maximum

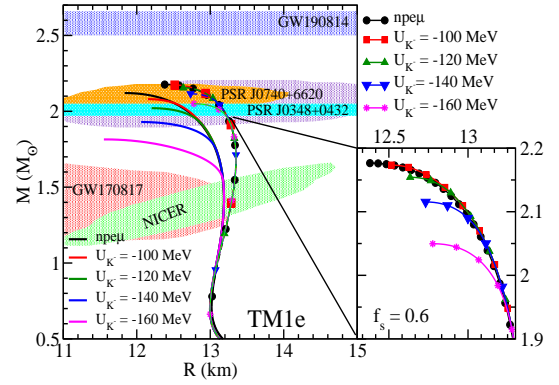


FIG. 9: Same as Fig. 8 but for TM1e.

TABLE III: The maximum mass, M_{max} (in units of M_\odot), radius (in km), corresponding central density (in units of n_0) of neutron stars for different values of antikaon optical potential depths U_{K^-} (in units of MeV) at n_0 for TM1 (upper panel) and TM1 with $f_s = 0.6$ (lower panel).

U_{K^-} (MeV)	M_{max} (M_\odot)	R (km)	$n_c(n_0)$
0	2.178	12.388	5.884
-100	2.156	12.683	5.641
-120	2.103	12.878	5.436
-140	2.005	12.970	5.354
-160	1.856	12.638	5.839
0	2.251	12.995	5.044
-100	2.250	13.058	5.051
-120	2.237	13.226	4.908
-140	2.201	13.398	4.726
-160	2.133	13.538	4.566

mass neutron star constraint of approximately $2M_\odot$ except -160 MeV for TM1 and except -140 and -160 MeV for TM1e, respectively. On the other hand, the radius corresponding to the maximum mass for all the values of U_{K^-} is below 13.0 and 13.6 km for TM1 and TM1 with $f_s = 0.6$ as given in Table III, respectively. Similarly, one can find from Table IV the radius corresponding to the maximum mass for all the values of U_{K^-} is below 12.3 and 12.8 km for TM1e and TM1e with $f_s = 0.6$, respectively. The equation of state (EoS) of TM1 and TM1e with $f_s = 0.6$ for all values of U_{K^-} satisfies the observed maximum mass constraint of $2M_\odot$. Overall, for a given depth of the (anti)kaon potential, TM1 and TM1 with $f_s = 0.6$ have a slightly higher maximum mass and radius compared to TM1e and TM1e with $f_s = 0.6$. This is because TM1e has a Λ_ν coupling, which makes the EoS softer at high densities.

The threshold densities n_{cr} for antikaon condensation in dense nuclear matter for different values of U_{K^-} along with corresponding mass and radius for TM1 and TM1 with f_s are shown in Table V. Similar results for TM1e and TM1e with f_s are given in Table VI. One can see from the observation of Tables V and VI that with an increase in the depth of the (anti)kaon potential, the threshold density n_{cr} for antikaon condensation and the corresponding mass decrease while the radius is increasing. This trend is consistent regardless of the

TABLE IV: The maximum mass, M_{max} (in units of M_\odot), radius (in km), corresponding central density (in units of n_0) of neutron stars for different values of antikaon optical potential depths U_{K^-} (in units of MeV) at n_0 for TM1e (upper panel) and TM1e with $f_s = 0.6$ (lower panel).

U_{K^-} (MeV)	M_{max} (M_\odot)	R (km)	n_c (n_0)
0	2.120	11.836	6.273
-100	2.080	12.151	5.951
-120	2.021	12.202	5.889
-140	1.929	12.060	6.112
-160	1.815	11.553	6.951
0	2.176	12.380	5.420
-100	2.173	12.516	5.335
-120	2.154	12.634	5.196
-140	2.115	12.732	5.065
-160	2.050	12.777	4.982

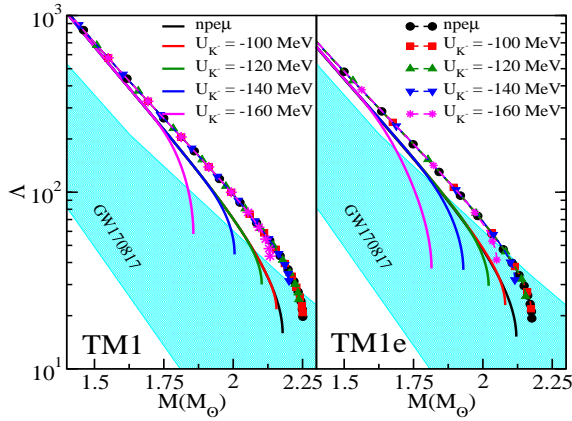


FIG. 10: The left panel displays the tidal deformability (Λ) of a neutron star as a function of mass for the TM1 model, while the right panel shows the predictions of the TM1e model. Solid lines in both panels represent calculations without the σ -cut, while those with symbols are with a σ -cut ($f_s = 0.6$) scheme. The neutron, proton, and lepton matter are represented by black lines, whereas others denote K^- condensates for different U_{K^-} potentials. The shaded region indicates the available astrophysical constraints.

TABLE V: The threshold densities, n_{cr} (in units of n_0) for antikaon condensation in dense nuclear matter for different values of U_{K^-} (in units of MeV) at n_0 . The corresponding mass M (in units of M_\odot) and radius (in km) of neutron stars for TM1 (upper panel) and TM1 with $f_s = 0.6$ (lower panel).

U_{K^-} (MeV)	n_{cr} (n_0)	M (M_\odot)	R (km)
-100	4.436	2.125	13.090
-120	3.725	2.025	13.504
-140	3.160	1.875	13.847
-160	2.850	1.705	14.091
-100	4.692	2.248	13.155
-120	4.064	2.219	13.463
-140	3.518	2.151	13.756
-160	3.032	2.026	14.018

TABLE VI: The threshold densities, n_{cr} (in units of n_0) for antikaon condensation in dense nuclear matter for different values of U_{K^-} (in units of MeV) at n_0 . The corresponding mass M (in units of M_\odot) and radius (in km) of neutron stars for TM1e (upper panel) and TM1e with $f_s = 0.6$ (lower panel).

U_{K^-} (MeV)	n_{cr} (n_0)	M (M_\odot)	R (km)
-100	4.213	2.013	12.674
-120	3.552	1.874	12.951
-140	3.123	1.723	13.100
-160	2.776	1.532	13.178
-100	4.630	2.164	12.694
-120	4.037	2.118	12.937
-140	3.523	2.033	13.144
-160	3.077	1.894	13.293

parameter sets used. From Tables V and VI, one can observe that antikaon appears at the lowest density for $U_{K^-} = -160$ MeV irrespective of the parameter sets. It is to be noted that there is a slight variation in the value of n_{cr} and corresponding mass and radius for different values of U_{K^-} for TM1 and TM1e as well as TM1 and TM1e with f_s . For a given value of U_{K^-} , the TM1e and TM1e with f_s predict a smaller value of mass compared to TM1 and TM1 with f_s . This is due to the Λ_v coupling which makes the EoS softer at high densities. From Table V, we find that the mass corresponding to n_{cr} is above $2M_\odot$ for $U_{K^-} = -100$ and -120 MeV for TM1 (upper panel). But for TM1 with $f_s = 0.6$ (lower panel), the mass corresponding to n_{cr} is above $2M_\odot$ for all values of U_{K^-} . Similarly, as TM1e has a Λ_v coupling, only $U_{K^-} = -100$ MeV predicts the mass approximately $2M_\odot$ and TM1e with $f_s = 0.6$ (lower panel) the mass corresponding to n_{cr} is above $2M_\odot$ except $U_{K^-} = -160$ MeV. The σ -cut potential has an impact on the mass corresponding to n_{cr} , but the variation in n_{cr} , corresponding mass, and radius for different values of U_{K^-} is not significant.

In Fig. 10, we present the results obtained for the tidal deformability of the models considered here. It is known that in the final stages of the coalescence, neutron stars develop a mass quadrupole due to the extremely strong tidal gravitational field induced by the counterpart comprising the binary. The dimensionless tidal deformability describes the degree of deformation of a neutron star and depends on the nature of the equation of state (EoS) [66, 80–82]. In this regard, several bounds on the tidal deformability parameter ‘ $\Lambda_{1.4}$ ’ (at mass $1.4M_\odot$) have been calculated lately from different wavelength analyses of the GW170817 data. For example there is the lower limit $\Lambda_{1.4} > 344$ [83, 84] as well as the upper limits of $\Lambda_{1.4} < 800$ [78]. From the plot in Fig. 10, overall we can see that both models, TM1 and TM1e, agree with the shaded area of the GW analysis over Λ vs Mass, more so when condensates are not considered. However, TM1e results with (anti)kaon condensate at various potentials seem to be in better agreement with the data than that obtained with TM1. The impact of the condensate appears much later for the two models, and therefore, for all the schemes adopted in this work, we obtain $\Lambda_{1.4} = 900$ and 690 for TM1 and TM1e, respectively, which is more or less consistent with the upper and

lower bounds discussed earlier. Overall results from TM1e seem to be quite impressive with or without invoking the σ -cut scheme at all (anti)kaon potentials. The inclusion of the condensates, however, seems to lower the tidal deformability with an increase in mass.

IV. CONCLUSIONS AND SUMMARY

We adopt the σ -cut scheme, inevitably meant to stiffen the underlying EoS, thereby increasing the maximum mass obtained for neutron stars compared to well-known RMF models, TM1 and TM1e and investigate the effect of the same for neutron stars with (anti)kaon condensate obtained with different (anti)kaon optical potentials. The main difference between TM1 and TM1e is the density dependence of symmetry energy. From our present analysis, we found that TM1 and TM1e as well as TM1 and TM1e with σ -cut potential are consistent with a speed of sound (CS) model and a piecewise polytropic (PP) model. The role of the symmetry energy associated with the two models is highlighted with the global properties of the neutron stars such as maximum mass, radius, composition and tidal deformability and compared with the constraints imposed from other theoretical studies and observational data. The effect of the σ -cut scheme on the EoS is found to appear at $\approx 2n_0$ and increases thereafter. The K^- condensates start to appear at about $3.5n_0$, contributing to the overall charge neutrality of the matter and dominating

the population of other species thereby leading to deleptonization in matter as well. The appearance of the condensate is set earlier if the potential is deeper. We could obtain neutron star mass $M > 2M_\odot$ with the scheme for most of the K^- potentials considered here, which agrees with the recent observation of high mass stars such as *PSR J0740 + 6620* and *PSR J0348 + 0432*. The calculated tidal deformability parameter is also found to be in agreement with GW data analysis, particularly for the TM1e case.

In the present analysis, we set the value of the free parameter f_s to maintain the properties of finite nuclei in the TM1 model without being influenced by the σ -cut potential. Our analysis highlights the significance of the σ -cut scheme in achieving a maximum mass for neutron stars above $2M_\odot$, but it tends to over-estimate the corresponding tidal deformability of neutron stars. To address this discrepancy and incorporate constraints from other observational data related to the density dependence of symmetry, such as the low tidal deformability of neutron stars, it is necessary to include the ω - ρ (Λ_ν) coupling in the model. This aspect is clearly demonstrated in our TM1e results, emphasizing the importance of incorporating both the σ -cut potential and ω - ρ couplings for better alignment with observational constraints, particularly for neutron stars with non-nucleonic composition [85]. It is important to constrain the value of f_s which is constrained by theoretical studies and observational data in a model-independent manner using a Bayesian approach.

-
- [1] J. M. Lattimer and M. Prakash, *Science* **304**, 536 (2004).
 - [2] J. M. Lattimer and M. Prakash, *Phys. Rep.* **442**, 109 (2007).
 - [3] M. Oertel, M. Hempel, T. Klähn, and S. Typel, *Rev. Mod. Phys.* **89**, 015007 (2017).
 - [4] V. A. Ambartsumyan, and G. S. Saakyan, *Sov. Astron.* **4**, 187 (1960).
 - [5] N. K. Gledndennning and S. A. Moszkowski, *Phys. Rev. Lett.* **67**, 2414 (1991).
 - [6] C. Wu and Z. Ren, *Phys. Rev. C* **83**, 025805 (2011).
 - [7] J. Schaffner and I. Mishustin, *Phys. Rev. C* **53**, 1416 (1996).
 - [8] T. K. Jha, H. Mishra, and V. Sreekanth, *Phys. Rev. C* **77**, 045801 (2008).
 - [9] N. K. Patra, B. K. Sharma, A. Reghunath, A. K. H. Das, and T. K. Jha, *Phys. Rev. C* **106**, 055806 (2022).
 - [10] V. B. Thapa and M. Sinha, *Phys. Rev. D* **102**, 123007 (2020).
 - [11] Guo-yun Shao and Yu-xin Liu, *Phys. Rev. C* **82**, 055801 (2010).
 - [12] H. Li, X. -L. Luo and H. -S. Zong, *Phys. Rev. D* **82**, 065017 (2010).
 - [13] S. Pal, M. Hanauske, I. Zakout, H. Stöcker and W. Greiner, *Phys. Rev. C* **60**, 015802 (1999).
 - [14] N. K. Gledndennning and J. Schaffner-Bielich, *Phys. Rev. Lett.* **81**, 4564 (1998).
 - [15] D. B. Kaplan and A. E. Nelson, *Phys. Lett. B* **175**, 57 (1986).
 - [16] A. E. Nelson and D. B. Kaplan, *Phys. Lett. B* **192**, 193 (1987).
 - [17] G. E. Brown, K. Kubodera, M. Rho and V. Thorsson, *Phys. Lett. B* **291**, 355 (1992).
 - [18] C. H. Lee, G. E. Brown and M. Rho, *Phys. Lett. B* **335**, 266 (1994).
 - [19] V. Thorsson, M. Prakash, and J. M. Lattimer, *Nucl. Phys. A* **572**, 693 (1994).
 - [20] P. J. Ellis, R. Knorren and M. Prakash, *Phys. Lett. B* **349**, 11 (1995).
 - [21] R. Knorren, M. Prakash and P. J. Ellis, *Phys. Rev. C* **52**, 3470 (1995).
 - [22] M. Prakash, I. Bombaci, M. Prakash, P. J. Ellis, J. M. Lattimer and R. Knorren, *Phys. Rep.* **280**, 1 (1997).
 - [23] S. Banik, and D. Bandyopadhyay, *Phys. Rev. C* **66**, 065801 (2002).
 - [24] H. Guo, B. Liu and J. Zhang, *Phys. Rev. C* **67**, 024902 (2003).
 - [25] D. P. Menezes, P. K. Panda and C. Providência, *Phys. Rev. C* **72**, 035802 (2005).
 - [26] C. Y. Ryu, C. H. Hyun, S. W. Hong and B. T. Kim, *Phys. Rev. C* **75**, 055804 (2007).
 - [27] P. Yue and H. Shen, *Phys. Rev. C* **77**, 045804 (2008).
 - [28] P. Demorest, T. Pennucci, S. Ransom, M. Roberts and J. Hessels, *Nature* **467**, 1081 (2010).
 - [29] Z. Arzumanyan, et al., (NANOGrav Collaboration), *Astrophys. J. Suppl. Series* **235**, 37 (2018).
 - [30] J. Antoniadis, et al., *Science* **340**, 6131 (2013).
 - [31] E. Fonseca, et al., *Astrophys. J. Lett.* **915**, L12 (2021).
 - [32] T. E. Riley, et al., *Astrophys. J. Lett.* **918**, L27 (2021).
 - [33] J. -L. Jiang, S.-P. Tang, Y.-Z. Wang, Y.-Z. Fan, and D.-M. Wei, *Astrophys. J.* **892**, 55 (2020).
 - [34] C. Ducoin, J. Margueron, and C. Providência, *Europhys. Lett.* **91**, 32001 (2010).
 - [35] J. M. Lattimer and M. Prakash, *Phys. Rep.* **621**, 127 (2016).
 - [36] M. Centelles, X. Roca-Maza, X. Viñas and M. Warda, *Phys. Rev. Lett.* **102**, 122502 (2009).

- [37] F. J. Fattoyev, J. Piekarewicz, and C. J. Horowitz, *Phys. Rev. Lett.* **120**, 172702 (2018).
- [38] M. B. Tsang, et al., *Phys. Rev. C* **86**, 015803 (2012).
- [39] J. M. Lattimer and Y. Lim, *The Astrophys. J.*, **771**, 51 (2013).
- [40] J. M. Lattimer, and A. W. Steiner, 2014, *Eur. Phys. J. A* **50**, 40 (2014).
- [41] X. Roca-Maza, X. Vñas, M. Centelles, B. K. Agrawal, G. Coló, N. Paar, J. Piekarewicz, and D. Vretenar, *Phys. Rev. C* **92**, 064304 (2015).
- [42] I. Tews, J. M. Lattimer, A. Ohnishi, and E. E. Kolomeitsev, *Astrophys. J.* **848**, 105 (2017).
- [43] D. Adhikari, et al., (PREX Collaboration) *Phys. Rev. Lett.* **126**, 172502 (2021).
- [44] B. T. Reed, F. J. Fattoyev, C. J. Horowitz, and J. Piekarewicz, *Phys. Rev. Lett.* **126**, 172503 (2021).
- [45] H. Shen, F. Ji, J. Hu, and K. Sumiyoshi, *Astrophys. J.* **891**, 148 (2020).
- [46] Y. Sugahara and H. Toki, *Nucl. Phys. A* **579**, 557 (1994).
- [47] Prashant Thakur, B. K. Sharma, A. Ashika, S. Srivishnu, and T. K. Jha, *Phys. Rev. C* **109**, 025805 (2024).
- [48] Y. Zhang, J. Hu, and P. Liu, *Phys. Rev. C* **97**, 015805 (2018).
- [49] K. Sumiyoshi, K. Nakazato, H. Suzuki, J. Hu and H. Shen, *Astrophys. J.* **887**, 110 (2019).
- [50] S. S. Bao and H. Shen, *Phys. Rev. C* **97**, 015807 (2014).
- [51] B. G. Todd-Rutel and J. Piekarewicz, *Phys. Rev. Lett.* **95**, 122501 (2005).
- [52] K. A. Maslov, E. E. Kolomeitsev, and D. N. Voskresensky, *Phys. Rev. C* **92**, 052801(R) (2015).
- [53] S. Pal, C. M. Ko, Zi-wei Lin and B. Zhang, *Phys. Rev. C* **62**, 061903(R) (2000).
- [54] G. -Q. Li, C. H. Lee, and G. E. Brown, *Nucl. Phys. A* **625**, 372 (1997).
- [55] T. Waas and W. Weise, *Nucl. Phys. A* **625**, 287 (1997).
- [56] V. Koch, *Phys. Lett. B* **337**, 7 (1994).
- [57] M. Lutz, *Phys. Lett. B* **426**, 12 (1998).
- [58] A. Ramos and E. Oset, *Nucl. Phys. A* **671**, 481 (2000).
- [59] L. Tolos, A. Ramos, and A. Polls, *Phys. Rev. C* **65**, 054907 (2002).
- [60] E. Friedman, A. Gal, and J. Mares, *Phys. Rev. C* **60**, 024314 (1999).
- [61] R. Oppenheimer and G. M. Volkoff, *Phys. Rev.* **55**, 374 (1939).
- [62] R. C. Tolman, *Phys. Rev.* **55**, 364 (1939).
- [63] P. G. Krastev and F. Sammarruca, *Phys. Rev. C* **74**, 025808 (2006).
- [64] È. È. Flanagan and T. Hinderer, *Phys. Rev. D* **77**, 021502 (2008).
- [65] T. Hinderer, *Astrophys. J.* **677**, 1216 (2008).
- [66] T. Hinderer, B. D. Lackey, R. N. Lang and J. S. Read, *Phys. Rev. D* **81**, 123016 (2010).
- [67] T. Damour, A. Nagar, and L. Villain, *Phys. Rev. D* **85**, 123007 (2012).
- [68] S. Postnikov, M. Prakash, and J. M. Lattimer, *Phys. Rev. D* **82**, 024016 (2010).
- [69] M. Leonhardt, M. Pospiech, B. Schallmo, J. Braun, C. Drischler, K. Hebeler, and A. Schwenk, *Phys. Rev. Lett.* **125**, 142502 (2020).
- [70] P. Danielewicz, R. Lacey, and W. G. Lynch, *Science* **298**, 1592 (2002).
- [71] S. Huth, C. Wellenhofer, and A. Schwenk, *Phys. Rev. C* **103**, 025803 (2021).
- [72] T. E. Riley, et al., *Astrophys. J. Lett.* **887**, L21 (2019).
- [73] M. C. Miller, et al., *Astrophys. J. Lett.* **887**, L24 (2019).
- [74] G. Raaijmakers, et al., *Astrophys. J. Lett.* **887**, L22 (2019).
- [75] K. Hebeler, J. M. Lattimer, C. J. Pethick, and A. Schwenk, *Astrophys. J.* **773**, 11 (2013).
- [76] S. K. Greif, G. Raaijmakers, K. Hebeler, A. Schwenk, and A. L. Watts, *Mon. Not. Roy. Astron. Soc.* **485**, 5363 (2019).
- [77] G. Raaijmakers, et al., *Astrophys. J. Lett.* **893**, L21 (2020).
- [78] B. P. Abbott et al., (The LIGO Scientific Collaboration and the Virgo Collaboration), *Phys. Rev. Lett.* **119**, 161101 (2017).
- [79] B. P. Abbott et al., (The LIGO Scientific Collaboration and the Virgo Collaboration), *Phys. Rev. Lett.* **121**, 161101 (2018).
- [80] T. Damour and A. Nagar, *Phys. Rev. D* **80**, 084035 (2009).
- [81] T. Binnington and E. Poisson, *Phys. Rev. D* **80**, 084018 (2009).
- [82] Tuhin Malik, et al., *Phys. Rev. C* **98**, 035804 (2018).
- [83] D. Radice, A. Perego, F. Zappa, and S. Bernuzzi, *Astrophys. J. Lett.* **852**, L29 (2018).
- [84] A. Perego, D. Radice, and S. Bernuzzi, *Astrophys. J. Lett.* **850**, L37 (2017).
- [85] P. Ribes, A. Ramos, L. Tolos, C. Gonzalez-Boquera, and M. Centelles, *Astrophys. J.* **883**, 168 (2019).